

First principles predictions of magneto-optical data for semiconductor defects: the case of divacancy defects in 4H-SiC

Joel Davidsson,^{1,*} Viktor Ivády,^{1,2} Rickard Armiento,¹

N.T. Son,¹ Adam Gali,^{2,3} and Igor A. Abrikosov^{1,4}

¹*Department of Physics, Chemistry and Biology,
Linköping University, SE-581 83 Linköping, Sweden*

²*Wigner Research Centre for Physics, Hungarian Academy of Sciences,
PO Box 49, H-1525, Budapest, Hungary*

³*Department of Atomic Physics, Budapest University of Technology and Economics,
Budafoki út 8., H-1111 Budapest, Hungary*

⁴*Materials Modeling and Development Laboratory,
National University of Science and Technology 'MISIS', 119049 Moscow, Russia*

Abstract

Study and design of magneto-optically active single point defects in semiconductors are rapidly growing fields due to their potential in quantum bit and single photon emitter applications. Detailed understanding of the properties of candidate defects is essential for these applications, and requires the identification of the defects microscopic configuration and electronic structure. Multi-component semiconductors often host two or more non-equivalent configurations of point defects. These configurations generally exhibit similar electronic structure and basic functionalities, however, they differ in details that are of great importance whenever single defect applications are considered. Identification of non-equivalent configurations of point defects is thus essential for successful single defect manipulation and application. A promising way to identify defects is via comparison of experimental measurements and results of first-principle calculations. We investigate a possibility to produce accurate *ab initio* data for zero-phonon lines and hyperfine coupling parameters that are required for systematic quantum bit search. We focus on properties relevant for the possible use of the divacancy defect in quantum bits in 4H-SiC. We provide a decisive identification of divacancy configurations in 4H-SiC and clarify differences in prior predictions of 4H-SiC divacancy zero-phonon photoluminescence lines.

I. INTRODUCTION

The physics of semiconductor point defects is of outstanding importance for controlling their optical and electrical properties^{1,2}. The study of point defect properties is a field of much active interest due to recent discoveries of numerous magnetically and optically active defect centers that can act as a single photon source³⁻⁷ or a quantum bit (qubit)⁸⁻¹⁰. So far, the most thoroughly investigated point defect for use in qubits are the NV-center in diamond¹¹⁻¹⁴, phosphor in silicon¹⁵⁻¹⁷ and divacancy¹⁸⁻²⁰ in silicon carbide (SiC). Furthermore, numerous other centers in various semiconducting host materials are proposed as potential magneto-optical centers, such as silicon-vacancy and germanium-vacancy centers in diamond^{21,22}, silicon vacancy in SiC^{23,24}, carbon anti-site vacancy pair in SiC²⁵, Ce³⁺ and Pr³⁺ ions in yttrium aluminium garnet^{5,26}, Eu and Nd³⁺ ion in yttrium orthosilicate^{27,28}, Nd³⁺ yttrium orthovanadate²⁹, defect spins in aluminum nitride³⁰, etc.

To manipulate these centers on single defect level and to reconstruct their Hamiltonian, it is essential to identify the microscopic structure, electronic structure, and spin-configuration of the center. State-of-the-art experimental techniques used in experimental point defect investigation are for instance, photoluminescence (PL) or absorption spectroscopy, electron spin resonance (ESR), deep-level transient spectroscopy (DLTS), and Raman spectroscopy, that probe different characteristics of the centers. Gathering all the available information about a considered center can provide an appropriate working model. However, there are numerous unidentified defect centers in most of the commercially available semiconductors³¹.

In semiconductors where multiple non-equivalent sites exist in the primitive cells, each point defect can have several different configurations. These distinguishable configurations exhibit different properties and thus different applicability in qubit and single photon emitter applications. The identification of such non-equivalent configurations is particularly challenging. For the non-equivalent configurations of divacancy related qubits in 4H-SiC two contradictory identifications have been presented, which rely on either the calculated zero-phonon photoluminescence (ZPL) lines³² or the zero-field splitting parameter (ZFS)³³. Furthermore, recently more divacancy related centers were reported than the possible number of non-equivalent divacancy configurations in SiC^{18,19}, which makes the identification even more puzzling.

Identification and characterization of point defects are greatly facilitated by first principles theory. In supercell or cluster models, a small part of the material that embeds a single point defect is directly modeled in electronic structure calculations. This way many properties of the defects,

such as spectral properties, charge transition levels, ESR parameters can be obtained, etc. In the literature, one can find different strategies how these quantities can be obtained in first principles calculations^{34–38}. However, when comparing computational results to experiments, special care must be taken to account for numerical uncertainty and limitations in the theoretical methods³⁸. So far there has been limited discussion about how to generally achieve an accuracy sufficient for identification of non-equivalent defects. In the present paper, we address this issue.

We assess the accuracy of first principle calculations of ZPL and hyperfine interaction parameters to create guidelines for theoretical point defect calculations that allow non-equivalent defect configurations to be identified. In particular, we consider the divacancy defect in 4H-SiC and consistently identify PL1-PL4 room temperature qubits by comparing convergent magneto-optical data with the experiment. This defect has been studied with *ab initio* calculations before, but the present study helps clarifying previous results that (as discussed above) have not been fully consistent^{32,33}. However, a main purpose of the present investigation is also to identify a scheme capable of reliably generating data via high-throughput calculations^{39,40} useful for identification of, essentially, any previously unknown point defect. For this intended use, it is imperative to identify methods that reliably produce sufficiently accurate results, but also take minimal computational effort.

The rest of this paper is organized as follows. Section II describes the basic properties of SiC and divacancy point defect in 4H polytype of SiC. In Section III gives details on the first principle methods used in this work. Section IV presents the results and discussion of our first principles point defect calculations. In section V, we demonstrate how to use our results to identify divacancy configurations in 4H-SiC. Finally, section VI summarizes our findings.

II. DIVACANCY IN SiC

SiC is a polytypic semiconductor with more than 250 polytypes synthesized. The most commonly used forms are 3C, 4H, and 6H-SiC. The 3C polytype, shown in Fig. 1(a), has cubic symmetry with a single C and Si atom in the primitive cell. The 4H polytype, in Fig. 1(b), has hexagonal symmetry and 8 atoms in the primitive cell of which 2 are non-equivalent for both Si and C (see Fig. 1(a)). The 6H polytype is also of hexagonal symmetry, has 12 atoms in the primitive cell, and 3 are non-equivalent for both Si and C (see Fig. 1(c)). Hence, a single site defect in 4H has 2 distinguishable configurations, and 3 in 6H. A pair defect then has 4 and 6 configurations, re-

spectively. The non-equivalent sites in 4H and 6H-SiC are referred to as h and k (4H), and h , k_1 , k_2 (6H). Here, h refers to a site in an hexagonal-like environment, and k to a cubic-like environment. In this paper, we focus on the four possible configurations of divacancy in 4H-SiC; hh , kk , hk , and kh , where the $V_{\text{Si}}-V_{\text{C}}$ notation is used. For two of these configurations, hh and kk , the $V_{\text{Si}}-V_{\text{C}}$ axis of the defect is parallel to the hexagonal axis of 4H-SiC and possess C_{3v} point group symmetry. The other two, hk and kh , have lower C_{1h} symmetry. hh and kk configurations are often called as axial configurations, while hk and kh as basal configurations.

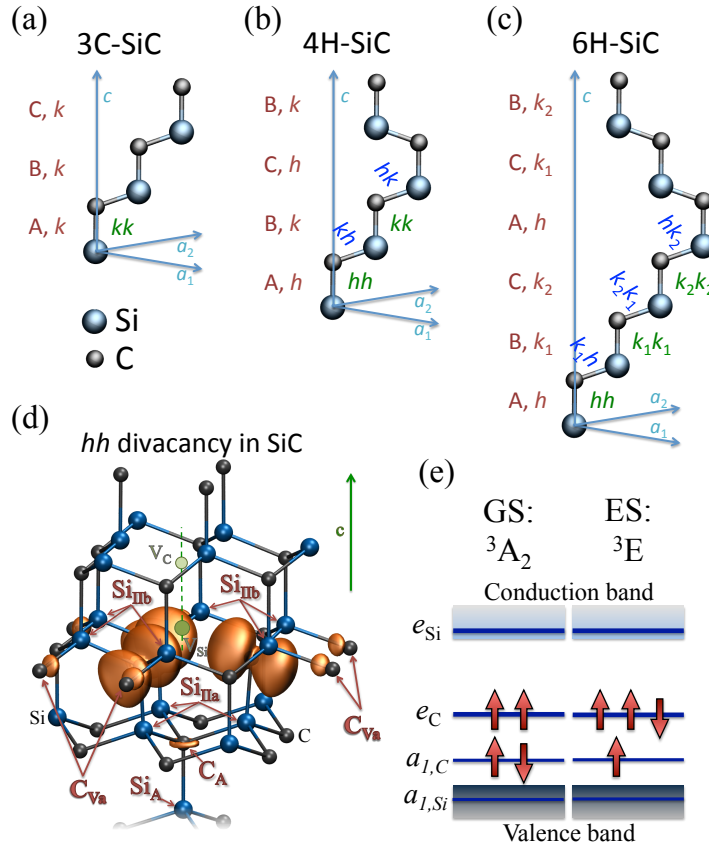


FIG. 1: Structure and configuration of defects in SiC. Fig (a-c) show the primitive cells of 3C, 4H, and 6H-SiC. Red upper-case letters show the stacking of Si-C double layers, while lower-case letters shows whether the double layers and their immediate surroundings follow a cubic like (k) or in a hexagonal-like (h) stacking order. Green lower-case letter pairs show variants of a pair defect. Figure (d) depicts hh divacancy configuration in 4H-SiC, the spatial distribution of the spin density (orange lobes), and the important neighboring Si and C sites that can give rise to notable hyperfine interaction. Figure (e) schematically shows the occupancy of single-particle orbitals in the ground and excited states of the divacancy.

Due to the C_{3v} symmetry in hh and kk , the dangling bonds of silicon and carbon vacancies form two fully symmetric a_1 and two double degenerate e states, which are occupied by 6 electrons⁴¹. The a_1 states are fully occupied, with the one localized on the silicon dangling bonds falling into the valence band, while the other one is localized on the carbon atoms and appears in the band gap of 4H-SiC near the conduction band edge. The e state is localized on the carbon dangling bonds and is located in the middle of the band gap and occupied by two electrons with parallel spin in the spin-1 ground state the divacancy. The other empty e state falls into the conduction band, as shown in Fig. 1(e). In the case of basal configurations, the low symmetry crystal field splits the e states into a' and a'' and transforms a_1 to a' .

Due to the spin-1 ground state and localized nature of the defect states, a strong dipole-dipole interaction can be observed between the unpaired electrons which causes a splitting of the spin sublevels even at zero magnetic field. For the divacancy defect, this zero-field-splitting is approximately 1.3 GHz. In SiC there are two intrinsic paramagnetic nuclei, the spin-1/2 ^{13}C with 1.07% natural abundance and the spin-1/2 ^{29}Si with 4.68% natural abundance, which can interact with the spin of divacancy and cause hyperfine structure in ESR spectrum. The spin density and important nuclei sites which yields resolvable hyperfine splitting of 10 – 100 Mhz are shown in Fig. 1(d).

In the single particle picture, the optically excited state of lowest energy can be constructed by a spin conserving promotion of the electron from the higher a_1 state to the e state, see Fig. 1(e). Due to the partial occupancy of the e_C state, the excited state is Jahn-Teller unstable, which causes spontaneous distortion of the atomic configurations of axial divacancies. In the many particle picture, six multiplets form in the triplet excited state that split according to the spin-spin and spin-orbit interactions. The divacancy in 4H and 6H-SiC has an electronic configuration similar to that of the divacancy and NV-center in diamond^{11,18,41,42}, thus the many particle picture derived for the NV-center⁴²⁻⁴⁴ can be applied for the divacancy too.

The experimental divacancy related ZPL lines are named the UD-2 group³¹ and PL1-4 lines^{18,19}, the electron spin resonance lines as P6/P7 centers^{45,46}.

III. METHODOLOGY

The ZPL line is the energy difference between the ground state and excited state. These states can be seen in Fig. 1(e). The energy is obtained by using Kohn-Sham (KS) density functional theory^{47,48} (DFT). In the excited state calculation, constrained occupation DFT scheme⁴⁹ is ap-

plied, and accordingly a KS particle is promoted from the a_1 state to the empty e state in the minority spin channel and self-consistent energy minimization, including geometry relaxation, is carried out. In *absolute values*, one cannot expect better than 100 meV accuracy from this scheme, due to the single Slater determinant description of the excited state. This uncertainty of the theoretical method is an order of magnitude larger than the accuracy requirement of non-equivalent configuration identification (10 meV, which is the typical difference of ZPL energies for the divacancy defect). On the other hand, as the crystal field potential differs qualitatively only from the second neighbor shell and the defect state localization is decaying exponentially in this region, the electronic structure of the non-equivalent configurations can be considered as nearly identical. Hence, ZPL energy differences follow from the potential perturbations acting on the defect orbitals. Therefore, to identify the non-equivalent configurations, our DFT calculations must capture those effects that are caused by a perturbing crystal field potential. As the potential has a direct effect on the density and energy, such identification is likely to be possible through DFT ZPL energy calculations. In other words, for *relative differences* of the ZPL energies, one may expect better than 100 meV in constrained occupation DFT calculations. In the following, this topic is investigated in details by assessing technical and theoretical limitations of ZPL energy calculations.

We apply three exchange-correlation functionals in our calculations; the semi-local functionals of Perdew, Ernzerhof, and Burke (PBE)⁵⁰ and of Armiento and Mattsson (AM05)⁵¹; and the screened hybrid functional of Heyd, Scuseria, and Ernzerhof (HSE06)^{52,53}. The hybrid functional is computationally much more expensive than the semi-local functionals, however, the band gap of semiconductors are closer to experiment⁵⁴ and accurate results in hyperfine field⁵⁵ as well as in zero-phonon line calculations^{37,49}. All functionals are computed using the PBE pseudopotential labeled 05jan2001 for C and 08april2002 for Si.

The recommended procedure for the HSE06 hybrid functional is to start from a semi-local density, hence the following scheme is introduced. The ground state is converged by first running a ground state PBE calculation then ground state HSE06 calculation. For the excited state, first, an excited state PBE calculation is executed. Then, a single self-consistent ground state HSE06 calculation is performed to obtain a good starting wavefunction for the final HSE06 excited state calculation.

In practice, we employ the Vienna Ab initio Simulation Package (VASP)^{56,57}, which uses the plane wave basis set and the projector augmented wave (PAW)^{58,59} method to describe the KS

states and handle the effects of the core electrons. Since we need highly accurate results, we use comparatively high settings for those convergence parameters that are not further discussed in this study. The stopping criterion for the self-consistent field calculations and for the structural minimization are 10^{-6} eV respectively 10^{-5} eV (energy difference) for the PBE functional. For HSE06 functional, the settings are instead 10^{-4} eV and 10^{-2} eV/Å (force difference). The grid for the Fast Fourier transformation (FFT) is set to twice the largest wave vector in order to avoid wrap around errors. For the HSE06 functional, the FFT grid for the exact exchange is set to the largest wave vector. This produces some noises in the forces but good energies. The above-described settings ensure a numerical accuracy in the order of 1 meV for the calculated total energies. A Monkhorst-Pack⁶⁰ k-point grid is used for those calculations that use more k-points than the gamma point. In the rest this work, unit cell atom counts always refer to the number of atoms in a pristine supercell, if not otherwise specified.

The zero-point energy shift of the ZPL energies due to the different vibrational properties of the ground and excited states is assumed to be small enough to not interfere with our conclusions. It is neglected in the present study.

For hyperfine field calculations⁵⁵, we use the implementation included in VASP, which gives the hyperfine tensor that describes the interaction between nuclear spin and electronic spin. This interaction produces a small splitting in energy levels which can be measured in experiments.

For zero-field-splitting, we follow the method of Ref.⁶¹ that requires Kohn-Sham wavefunctions as obtained by VASP DFT calculations. Here, we use the plane wave part of PBE wavefunctions to calculate the zero-field splitting tensor, the one center contributions from the PAW potentials are neglected. This approximation give an error of a few percent in the calculated values.⁶¹

IV. ACCURATE POINT DEFECT CALCULATIONS

In this section, results from zero-phonon line energy, hyperfine field, and stress calculations are presented.

1. Supercell size

First, we demonstrate the convergence of ZPL energies on supercell size. We begin by using supercells that retain the hexagonal symmetry of the primitive cell, the PBE functional, and Γ -point

sampling of the Brillouin zone (BZ). We fixed the c -axis size of the supercell to 20.25 Å (twice of the primitive cell in that direction) and varied the lateral size of the cell in the basal directions. Figure 2 shows how the ZPL energies converge with increasing supercell sizes. With a supercell of 10×10 copies of the primitive cell in the basal directions (ca 31 Å in the a_1 - and a_2 -axis) the ZPL energies appear to converge to within 1 meV. Using this converged distance ≈ 30 Å in the c -direction as well gives a supercell ($10 \times 10 \times 3$) consisting of 2400 atoms. We will use the converged values at this size as a benchmark for with which to compare other methods.

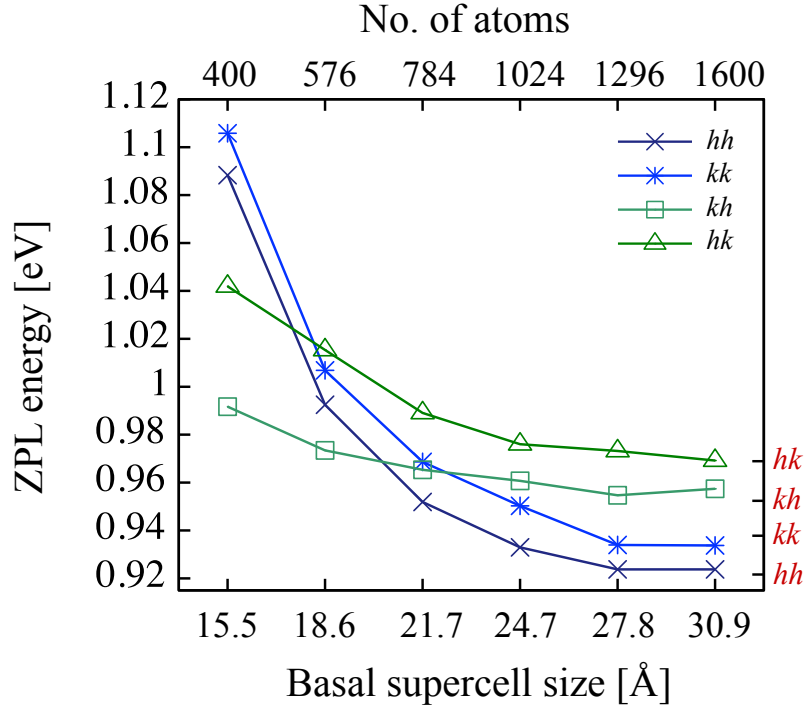


FIG. 2: Supercell size convergence of ZPL energies of divacancy configurations in 4H-SiC calculated with the PBE functional and a Γ -point only k-point grid. Scaling is carried out in hexagonal supercell only in the basal direction. The c -axis size of the supercell is fixed at 20.25 Å. The horizontal axis shows both the number of the atoms in the supercells and the basal plane lateral size of the supercell are provided. The right axis shows the converged ZPL for the 2400 supercell.

As one can see in Fig. 2, different configurations exhibit different convergence behavior. Axial configurations, hh and kk , are more sensitive to the supercell size in the basal plane than the low symmetry basal configurations, hk and kh . As divacancy defect states have their largest expansion in a plane perpendicularly to the symmetry of the axis of the defect (cf. Fig. 1) the observed

behavior can be explained by the overlap of the wavefunction of the defect and its periodically repeated images, due to the periodic boundary condition. The hh and kk defects extend most in the basal plane, thus, their self-overlap error sensitively depends on the basal plane lateral size of the supercell. For kh and hk the overlap is smaller, since these configurations have their largest expansion in a plane with an angle to the basal plane, thus they are less sensitive to the supercell size in the basal plane. It is clear that the ZPL energies only converges at very large supercell sizes.

Note that, the observed finite size dependence is a combination of several effects, including the convergence of the charge density of 4H-SiC, exponential decrease of the self-interaction wavefunction of the defect, and the relaxation of the strain caused by the defect as the supercell size is increased. In the following subsections, we investigate these effects separately.

2. Brillouin zone sampling

In contrast to the straightforward study above of the convergence of ZPL on supercell size in a Γ -only k-point calculation, we now turn to convergence in smaller cells with higher Brillouin zone sampling. While a smaller supercell will increase errors due to vacancy-vacancy interaction, the aim is to investigate if one can still reach results that are accurate enough with significantly less computational overhead. Fig. 3 shows the PBE ZPL energies for different supercells of hexagonal and rectangular symmetry. As can be seen, the level of BZ sampling is important for all the considered supercells. The order of the ZPL energies of the non-equivalent divacancy configurations largely depends on the k-point convergence. The 576 atom supercell requires a $2 \times 2 \times 2$ BZ sampling to provide the convergent order of PL lines, even though the absolute values are slightly smaller than for those convergent 2400 atom supercell.

Fig. 4 shows the final result after k-point convergence of different hexagonal and symmetric supercells. As can be seen, calculations with converged BZ sampling provide the same order for the ZPL line energies as the fully converged 2400 atom supercell for supercells of 96 atoms and larger. On the other hand, the absolute value of the ZPL energies can vary 50 - 100 meV with supercell size.

These results indicate that careful convergence in k-point density can produce the same order of ZPL energies for smaller supercells than calculations carried out with Γ -point sampling. The only exception is the hexagonal 72 atom supercell, where either the overlap of the defect states or the point defect caused stress turned to be ruinous.

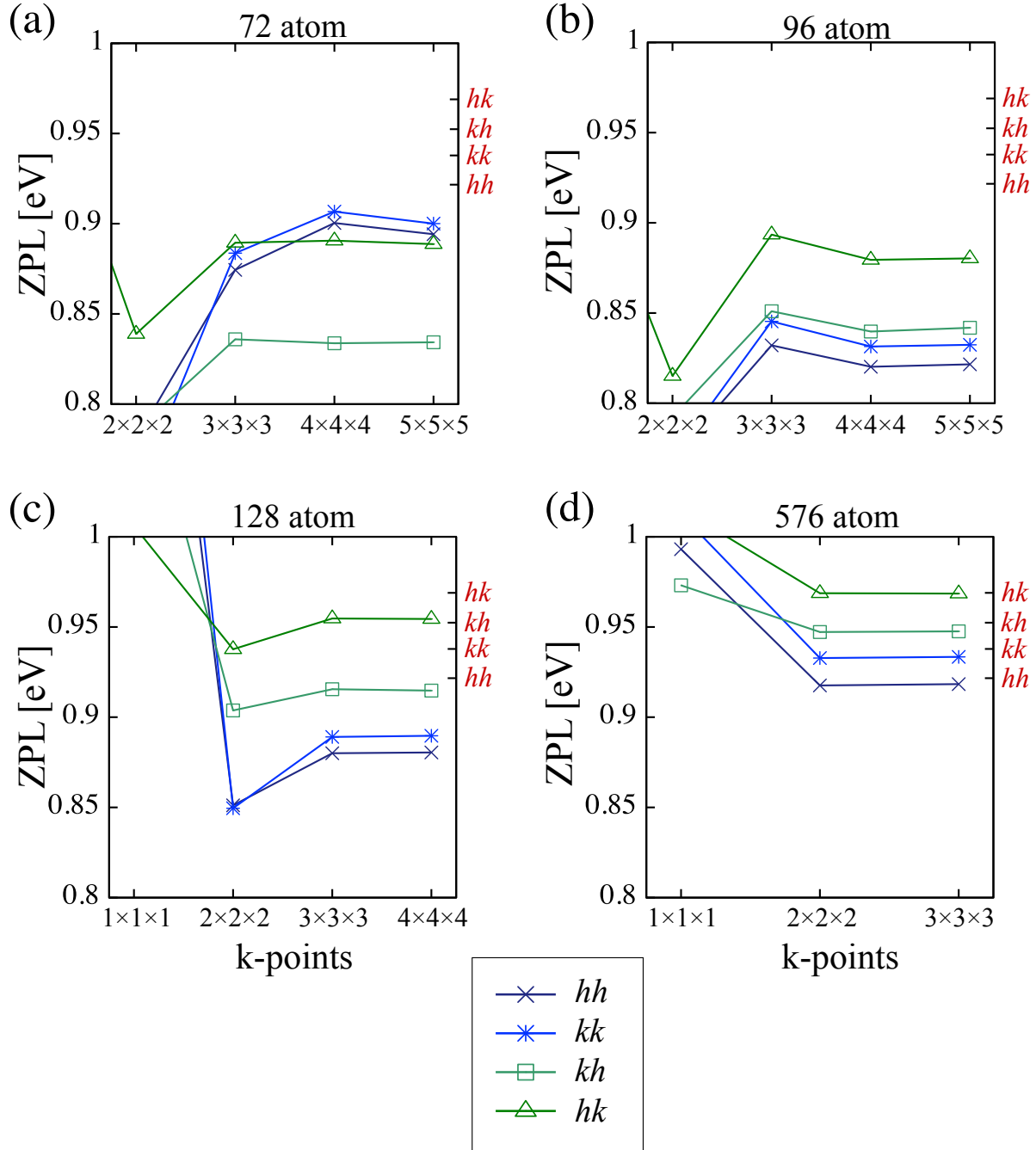


FIG. 3: Brillouin zone sampling convergence of ZPL energies for the divacancy defects in different supercell models of 4H-SiC. The right axis shows the converged ZPL for the 2400 supercell.

The presented calculations use a consistent k-point set between the relaxation and ZPL calculation. However, relaxations can be done using only the Γ -point, with a relative change of the ZPL of only 2%-4%. In contrast, the higher k-point sampling is critical for the ZPL energy calculations.

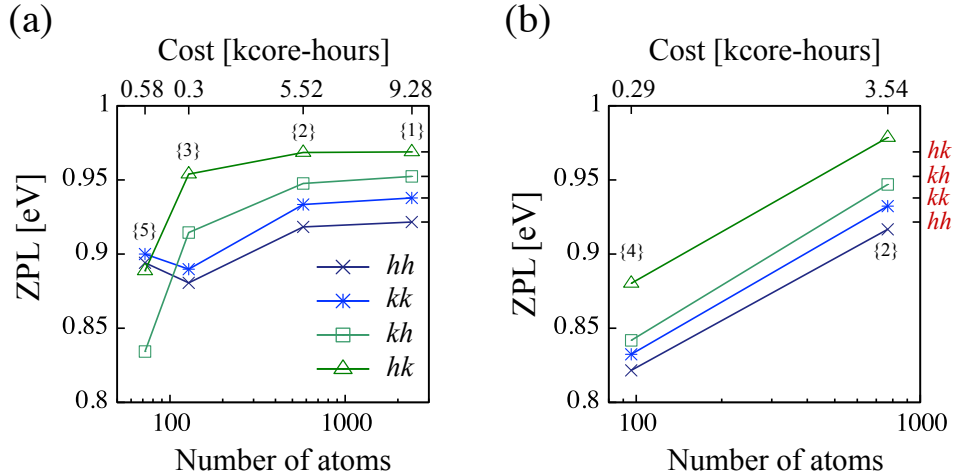


FIG. 4: K-point convergent divacancy ZPL energies for different (a) hexagonal and (b) rectangular, as close to cubic as possible, supercells. The right axis shows the converged ZPL for the 2400 supercell. Computational cost is shown on the top axis. $\{n\}$ means $n \times n \times n$ k-points. The presented core-hours are the total amount of computer time needed to calculate one ZPL value on a cluster with 2.2 GHz processors.

This may seem surprising at first, but we speculate that the widening of the bands beyond the zero dispersion of the gamma calculation is important to reproduce the correct physics.

Next, we study the k-point convergence of the ZPL energies calculated by the HSE hybrid functional. Due to the large computational cost of hybrid calculations, we are unable to carry out a study of convergence as thorough as for PBE. Here, we investigate the BZ sampling convergence for the smallest supercell that is sufficient for reproducing the lines in right order. The results for cubic 96 atoms and hexagonal 128 atoms are presented in Fig. 5. As can be seen, the HSE06 functional exhibits similar k-point convergence as the PBE functional. The absolute values of the ZPL are about 0.2 eV larger for the computational heavy HSE06 functional than compared with the PBE functional, also the hh and kk switch order compared to the PBE results. The difference between the ZPL results for the 96 and 128 atoms supercell is smaller for the HSE06 functional than for the PBE functional. This would suggest that the HSE06 functional converges faster with respect to supercell size than the PBE functional.

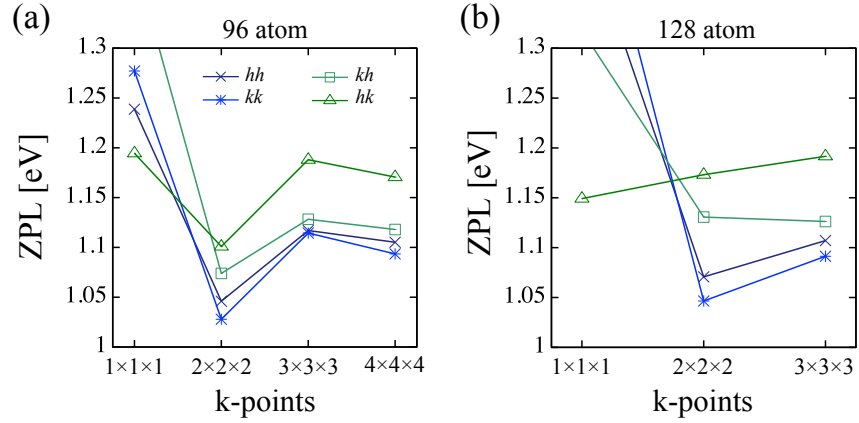


FIG. 5: Brillouin zone sampling convergence of the HSE06 ZPL energies of divacancy configurations in a rectangular 96 atoms and hexagonal 128 atoms supercell of 4H-SiC.

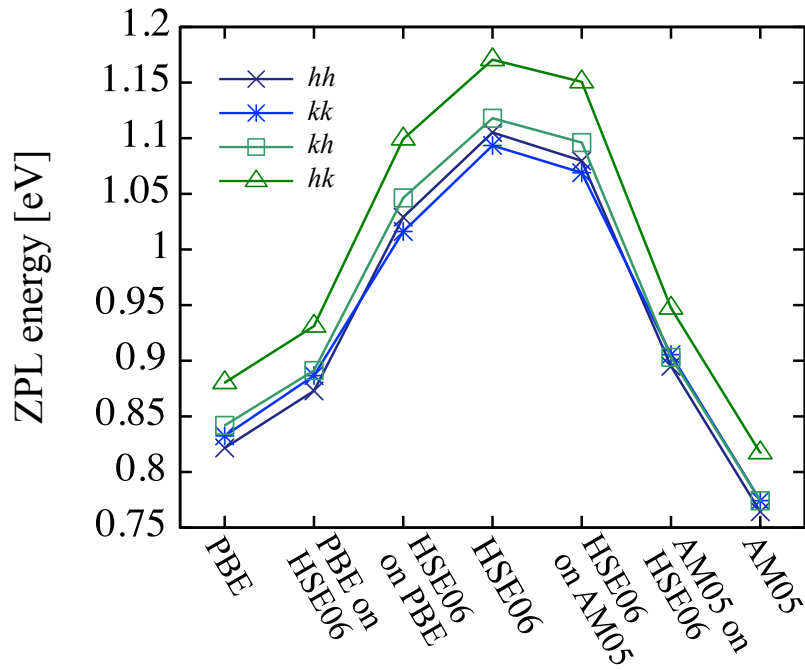


FIG. 6: Divacancy ZPL energies calculated with various functionals using different strategies. Values for PBE, AM05, and HSE06 have used those functionals for all steps in the calculation. Values specified as 'A on B' utilize the B functional for all relaxations, and the A functional for the final static calculation to determine the ZPL.

3. Functional and geometry dependence

Next, we investigate how the choice of the functional and the way how the geometry optimization is performed affect the calculated ZPL energies. Fig. 6 shows the results of PBE, AM05, and HSE06 ZPL calculations, as well as PBE, AM05, and HSE06 ZPL energies as obtained on different geometries, i.e. PBE, AM05, or HSE06 relaxed structures. From these results, it is clear that the functional used for the relaxations has a smaller effect on the results than the functional used in the final static calculation of the ZPL energies. Most importantly, the functional used for relaxation does not change the order of the ZPL lines. While the functional, which is used to calculate the ZPL energies, has an important effect both on the absolute values as well as on the relative positions of the ZPL lines. Concerning the semi-local functionals, use of the PBE functional in all steps of the calculation brings the results closer to the HSE06 values compared to AM05. However, this appears to be related to a cancellation of error effect, since, as shown in Table I, the AM05 lattice constants are closer to the experimental ones than PBE.

In addition to the functionals shown in Fig. 6, we have also investigated the LDA functional and only comment on the results briefly. Somewhat surprisingly, the LDA results are in significant disagreement with the other functionals, with the final ZPL values of 1.50 for hh , 1.55 for hk , 1.50 for kh , and 0.87 for kk . Hence, LDA does not reproduce the experimental order, and, places one of the lines far from the others (0.7 eV away). This can be explained by the underestimated lattice parameter of LDA. Redoing the LDA calculation with the only difference of constraining the lattice constant during relaxation to the PBE value, gives results much closer in agreement with the others functionals (0.77, 0.83, 0.79, 0.78 for hh , hk , kh , and kk respectively). Hence, it appears an incorrect geometry specifically towards a too small lattice constant is disastrous for the end results. This warns against indiscriminate use of LDA in the determination of ZPL lines.

TABLE I: Lattice parameter for 4H-SiC for different functionals compared to experiment.

Lattice parameter	LDA	HSE06	Exp	AM05	PBE
a	3.059	3.071	3.073	3.077	3.094
c	10.015	10.052	10.053	10.070	10.125

4. Summary on ZPL line calculations

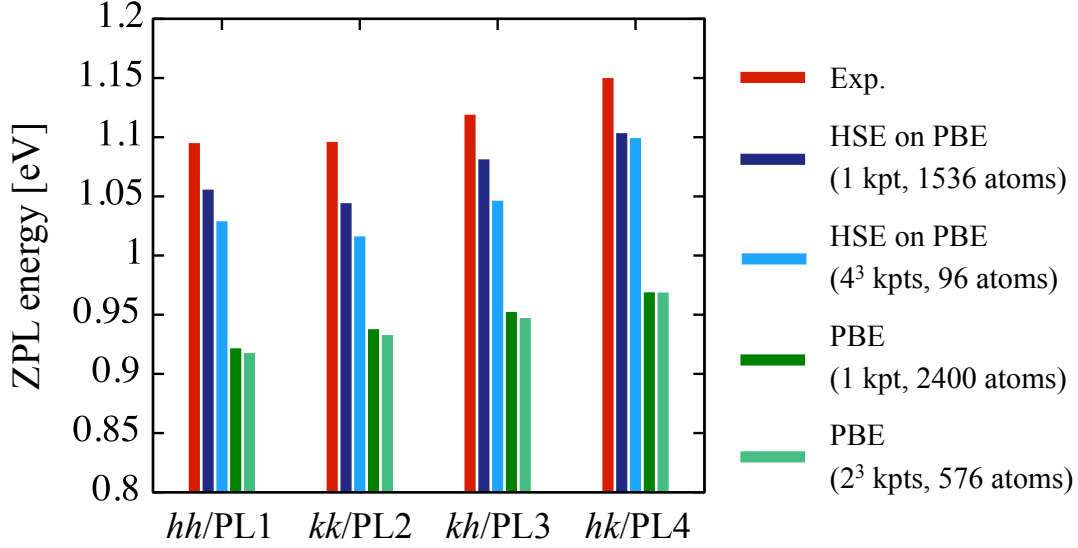


FIG. 7: Comparison of convergent theoretical ZPL energies with the experimental values¹⁹. Identification of the divacancy related PL centers in 4H-SiC is done based on the results of section V.

To summarize our results on ZPL calculations, we depict the experimental and theoretical results of different computational strategies in Fig. 7. Due to our findings in the previous section, relaxing the structure with PBE, or perhaps preferably AM05, combined with a single self-consistent HSE06 calculation is a fast alternative to running full relaxation with HSE06. As can be seen, in absolute terms the HSE06 functional provides excellent agreement with the experimental values even when PBE optimized geometries are used. PBE ZPL energies exhibit a notable finite-size effect, while the convergent values still fall 20% below the experimental and HSE06 values. Concerning the order of the PL lines, PBE and HSE06 functionals disagree in the order of the axial divacancy configurations in all the different computational approaches. On the other hand, the experimental energy difference between the axial, high symmetry configurations is only 1 meV, which cannot be achieved by any of ZPL energy calculations strategies, partially due to the neglect of the zero-point energy contribution. Therefore, we cannot decide if the HSE06 or the PBE functionals perform better in non-equivalent configuration identification based on ZPL energies. On the other hand, due to the non-local nature of HSE06 functional, it may provide a better description of the decaying region of the defect states with the rest of the defect states that can positively

affect the predicted order of the ZPL energies.

The decreased computational time from running PBE functional on 96 atoms (5500 core-hours) instead of 2400 atoms (9300 core-hours) is 40%. Running HSE on PBE for 1 k-point and 1536 atoms took approximately 36000 core-hours compared with HSE on PBE for $4 \times 4 \times 4$ k-points and 96 atoms which took approximately 27000 core-hours. This is a speedup of 25%. These core-hours are the total amount of computer time needed to calculate one ZPL value on a cluster with 2.2 GHz processors.

Finally, our results indicate that the computational cost of large HSE06 point defect calculations can be reduced substantially by using PBE or AM05 relaxed geometries with reasonable additional uncertainties both in the absolute values and relative differences of the ZPL energies.

A. Hyperfine field calculations

In this section, we discuss the methodological requirements needed for accurate hyperfine tensor calculations. As it was established previously, the most accurate values can be obtained by HSE06 functional including core state polarization effects⁵⁵. Previously, however, no supercell size and BZ sampling tests were carried out.

First, we investigate the k-point convergence of hyperfine tensor elements. We use the PBE functional and study different supercell sizes. In the tests we consider two hyperfine parameters, the isotropic Fermi-contact contribution, $A_{\text{Fc}} = (A_{xx} + A_{yy} + A_{zz}) / 3$, and the dipole-dipole splitting, $A_{\text{dd}} = |(A_{xx} + A_{yy}) / 2 - A_{zz}|$. The obtained convergence curves for a set of ²⁹Si and ¹³C sites close to a *hh* divacancy are depicted in Fig. 8. As one can see different sites exhibit different convergence behavior, which can be explained by the fact that the defect has different extension in different directions. In the basal plane, the extension is larger thus the defect states may require denser k-point grid in this direction. Furthermore, one can see that the criteria of complete convergence is similar to the criteria obtained for the ZPL energies.

Next, we investigate the supercell size dependence of A_{Fc} and A_{dd} hyperfine parameters. To do so we calculate the deviation of hyperfine parameters for numerous sites from the values obtained in a 2400 atom supercell calculation. In Fig. 9, relative errors of A_{Fc} and A_{dd} are shown for three smaller supercells. For all considered sites, the distance from the silicon vacancy site of the divacancy is also provided in the figure. As one can see, the relative error in the Fermi contact term increases dramatically with increasing distance of the divacancy and nuclear spins. Similar

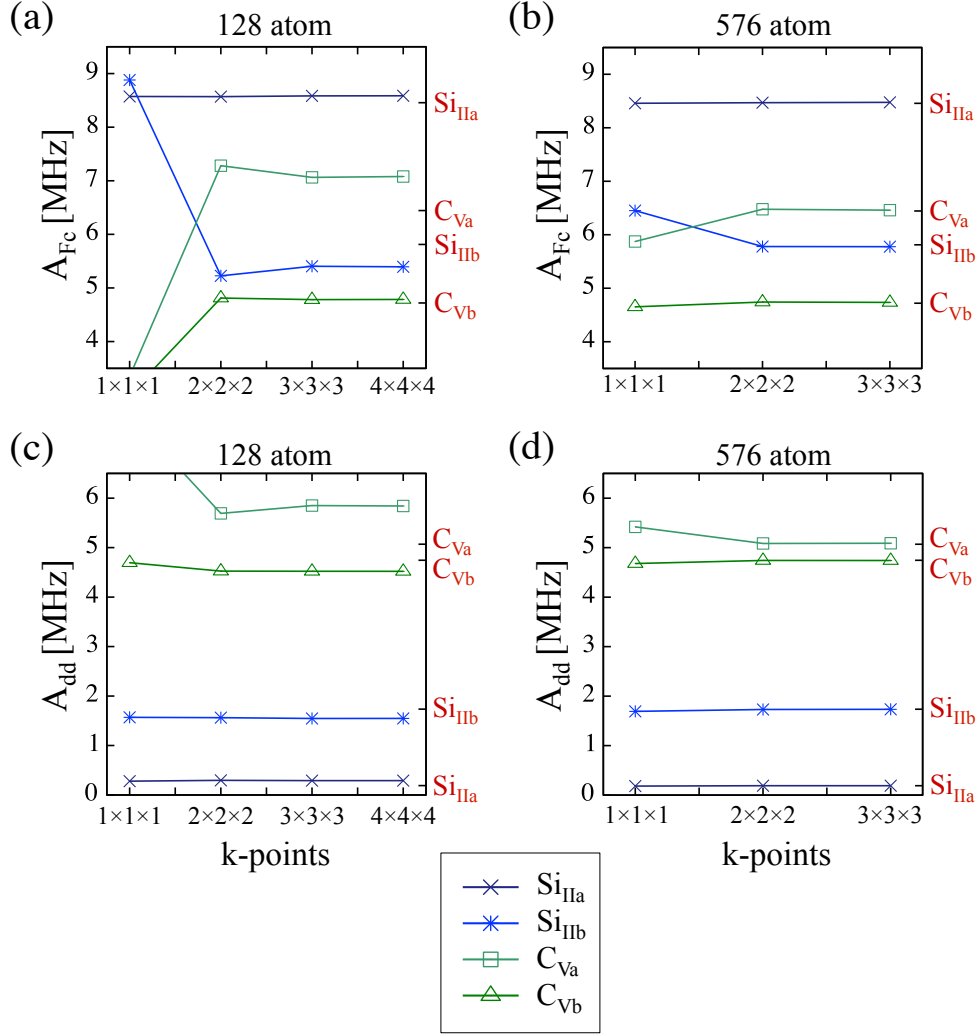


FIG. 8: Brillouin zone sampling grid size convergence of hyperfine parameters for different ^{29}Si and ^{13}C sites in 128 and 576 atom supercells. (a) and (b) show the Fermi contact parameter, while (c) and (d) show the dipole-dipole splitting for 128 and 576 atom supercells, respectively. The considered nuclei sites are marked in Fig. 1(d). The right axis shows the hyperfine parameters for the 2400 supercell.

tendency can be observed for the dipole - dipole hyperfine term. Furthermore, relative errors drastically decrease with increasing supercell size. The mean relative errors for different supercells are provided in Table II. Note that substantial errors were obtained even in the 128 atom supercell, while the 576 atom supercell results are nearly identical with the absolutely convergent 2400 atom supercell results. These observations can be explained by the overlap of the state from the defect and its replicas. As further hyperfine interaction of the nuclei sensitively depends on the

spin density localization in the farther neighbor shells, where defect state overlap can occur, they exhibit an enhanced finite size effect.

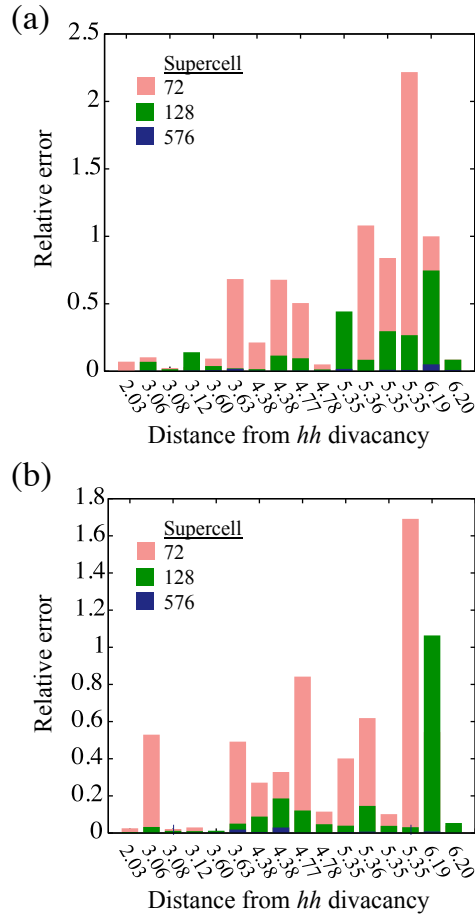


FIG. 9: Relative error of the calculated (a) Fermi contact and (b) dipole-dipole hyperfine interactions strength for various sites around a hh divacancy in 4H-SiC. On the horizontal axis, the distances of the considered sites from the silicon vacancy site of the divacancy are given. Calculations were carried out in 72, 128, and 576 atom supercell by using the PBE functional.

In summary, our results indicate that accurate hyperfine field calculations require supercells as large as 576 atoms or ≈ 20 Å lateral size. In smaller supercells, such as 128 atom supercell, only closest hyperfine field of the nuclei can be determined with reasonable accuracy.

B. Defect induced stress in supercell calculations

Point defects induce a distortion in their host crystal, which relaxes with increasing distances from the point defects. In finite supercell models, the size of the model is usually not sufficient to

TABLE II: Mean relative error (MRE) of the hyperfine interaction parameters presented in Fig. 9. Deviation measured from the hyperfine parameters obtained in absolutely convergent 2400 atom supercell calculations.

Supercell	MRE of A_{Fc} [%]	MRE of A_{dd} [%]
72	48.0	72.6
128	15.3	25.5
576	0.99	0.81

accommodate completely the induced strain field around a point defect, thus the atomic configuration of the defect cannot reach the single defect configuration in such calculations. This finite size effect also manifest itself as an artificial stress appears at the supercell surfaces. Here, we investigate how the induced stress relaxes with increasing supercell size.

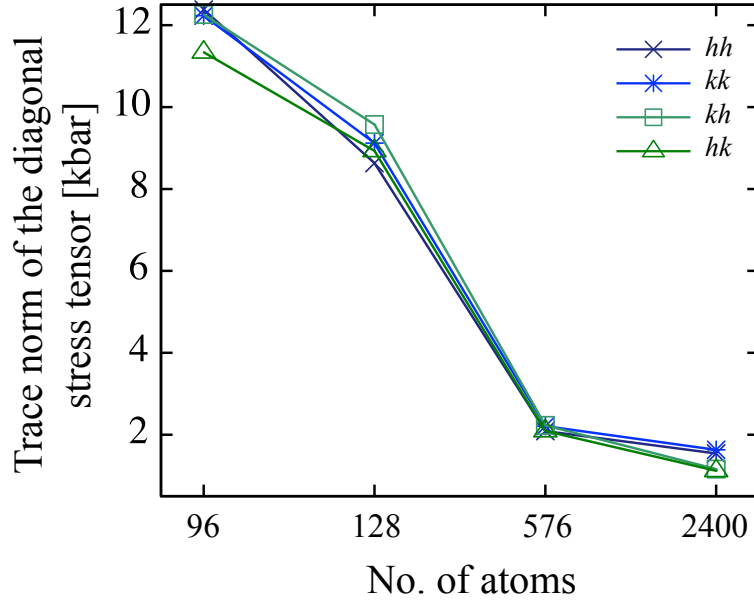


FIG. 10: Trace norm of the diagonalized stress tensor measured at the borders of different supercells of 4H-SiC embedding single divacancy defects.

As can be seen in Fig. 10, the stress indeed relaxes with increasing supercell size, however, it does not reach zero even in the largest 2400 atom supercell. Furthermore, the small difference

between the 576 and 2400 atom supercell results may suggest that 576 atom supercell is convergent in terms of stress.

In order to make a rough estimate how the observed stress affects the ZPL energies, we imagine that the NV center is subject to 10 kbar external pressure, which is approximately the difference of the stress observed in the smallest and largest supercells. By using the experimental pressure dependence of the ZPL energy, 0.575 meV/kbar ⁶², we obtain 5.75 meV. In SiC the effect could be larger, due to the smaller bulk modulus of SiC, however, presumably still remains in the order of 10 meV. Therefore, we conclude that the stress has a minor effect on the calculated ZPL energies.

V. IDENTIFICATION OF DIVACANCY RELATED ZERO-PHONON LINES IN 4H-SiC

In this section, we present an example of how accurate ZPL, ZFS, and hyperfine field splitting calculations can be used for identification of the divacancy configurations in 4H-SiC. We now consider a hypothetical case where one has been given the experimental ZPL lines in Table III for the four different defect configurations. Our aim is to identify the type of defect (vacancy, divacancy, interstitial, etc.), and match each line to a corresponding configuration (hh , hk , kh , and kk .)

First, the variation of ZPL energies between different defect types are usually on a scale > 100 meV. Hence, it should be straightforward to make the identification of defect type with access to k-point-converged results for HSE06 for the 96 atom unit cell with the geometry converged using PBE or AM05. Even the PBE results for 96 atom supercell could work to identify the defect type, even though the absolute error is larger, the relative error is on the same scale (cf. Fig. 3(b) and Fig. 5(a)). Next, we turn to the identification of the defect configuration corresponding to each line. The conclusion from the present work is that the accuracy of the ZPL energies with the methods described here are not of sufficient quality to identify the configurations from them alone (cf. Fig. 7). As has been discussed above, while PBE predicts the correct order for the ZPL, HSE06 does not. However, if we in addition to the ZPL also have experimental results for the ZFS and the hyperfine tensor, they can be used to aid the identification. These quantities require calculations using HSE06 with one k-point and a supercell converged in size (as described in Sec. IV A and Ref.^{55,61}). For the divacancy, we use 1538 atom supercell ($8 \times 8 \times 3$) with $24.7 \times 24.7 \times 30.4 \text{ \AA}^3$ volume, with Γ -point sampling. This calculation is converged in the c -axis direction and nearly converged in basal directions. To reduce the demand of such calculations, we use PBE relaxed

atomic configurations and single self-consistent HSE06 calculations. This calculation provides accurate hyperfine and ZFS results and also increases the accuracy of the ZPL lines. The results in Table III show that the added data and accuracy is sufficient to identify each line. The ZFS result for kh is far from experiment, this could be due to the neglect of the spin-orbit contribution.

Hence, we suggest a two-step process for defect identification. First, a database is needed for ZPL lines for all relevant defects and configurations, produced by PBE calculations for 96 atom supercells with $4 \times 4 \times 4$ BZ-sampling at a cost of 300 core hours/defect configuration on a cluster with 2.2 GHz processors. This database hopefully allows the identification of different defect type. Second, to identify the defect configuration requires additional calculations of ZFS and the hyperfine parameters. To produce accurate results, an HSE06 calculation on 1536 atom supercell, with Γ -point sampling, relaxed using PBE functional is needed. This also produces more accurate ZPL at a total cost of ca 35000 core hours/defect configuration.

To identify the defect, first, we chose an affordable but sufficiently accurate method to calculate all the necessary parameters. By studying the ZPL data presented in Fig. 7, one can identify kh and hk either from the PBE or HSE06 functional results. Even the results from a small supercell with high k-point set can identify the different configuration. But the hh and kk identification is conflicting between the functionals, then one needs other properties such as ZFS or hyperfine tensor to be sure. As we have seen, the HSE06 functional is required for accurate hyperfine tensor calculations⁵⁵ and also provides better results for the ZPL energies, due to its non-local nature. Furthermore, large supercells have many advantages that affect all the considered quantities and are needed for calculating accurate hyperfine tensor, even doe they are more computational demanding. Here, we use 1538 atom supercell ($8 \times 8 \times 3$) with $24.7 \times 24.7 \times 30.4 \text{ \AA}^3$ volume, with Γ -point sampling. This calculation is convergent in the c -axis direction and nearly convergent in basal directions. In this non-completely convergent calculations small uncertainties are expected, e.g. 10 meV in the ZPL energies, see Fig. 2, especially when axial and basal configurations are compared. To reduce the demand of such calculations, we use PBE relaxed atomic configurations and single self-consistent HSE06 calculations. ZFS is calculated using the method presented in Ref.⁶¹. This property is assumed to have the same convergence as hyperfine field. The results of these calculations are summarized in Table III.

Comparing with prior work, our identification agrees with that by Falk *et al.*³³, which uses the ZFS parameter and *ab initio* simulations. The ZFS parameter was calculated using the data from a 1200 atom supercell, with Γ -point sampling, using the PBE functional. Our computational results

TABLE III: Identification of divacancy related PL and ESR centers in 4H-SiC.

Configuration	PL line ^{18,19}	ESR ^{45,46}	Calc. ZPL	Exp. ZPL ¹⁹	Calc. ZFS	Exp. ZFS ¹⁹	Calc. A_z	Exp. A_z ⁶³
<i>hh</i>	PL1	P6b	1.056	1.095	1.329	1.336	9.06	9.2
<i>kk</i>	PL2	P6'b	1.044	1.096	1.307	1.305	9.99	10.0
<i>kh</i>	PL3	P7'b	1.081	1.119	1.314	1.222	–	–
<i>hk</i>	PL4	P7b	1.103	1.150	1.363	1.334	–	–

also agree with a calculation by Gordon *et al.*³² using the HSE06 functional on a 96 atom supercell with $2 \times 2 \times 2$ k-point grid. As the authors remarked it is not possible to use only ZPL to identify the different configurations due to the low accuracy of the calculations. The HSE06 functional predicts the wrong order and as discussed in the present work more accurate calculations do not resolve this but additional properties is needed for a correct identification.

VI. SUMMARY

This work discusses how to appropriately use *ab initio* calculations to facilitate identification of defect types and configurations in semiconductors. Specifically, we have shown how to correctly identify the different non-equivalent divacancy configurations in 4H-SiC using ZPL, ZFS, and hyperfine field splitting calculations.

The value and order of the zero-phonon lines are dependent on the choice of functional, the way the geometry is optimized, supercell size, and k-points density. A comparably small supercell that has been converged with respect to the number of k-points produces sufficient accurate results at lower computational cost than the typical setup of a large supercell with one k-point. The absolute value of the zero-phonon line energy depends strongly on the lattice constant. A smaller lattice constant gives larger zero-phonon line energy and vice versa. The functional affects both the order and absolute value. It turns out that using only ZPL data is not enough to successfully identify the different non-equivalent configurations, but ZFS and hyperfine field can provide additional information.

For hyperfine field, the size of the supercell is the most important factor. Close to the defect, the values do not vary as the supercell size changes. But as the supercell size decreases, the hyperfine field gets less accurate the further away from the defect one calculates it.

The approach that produces both most accurate zero-phonon lines and hyperfine field values, at an affordable cost, is to use a large enough supercell that only Γ -point sampling is needed, relax it with PBE or AM05 functional, and run a single self-consistent HSE06 calculation. Using this proposed algorithm, we have shown how to correctly identify the different non-equivalent divacancy configurations in 4H-SiC.

ACKNOWLEDGMENTS

Support from the Swedish Government Strategic Research Areas in Materials Science on Functional Materials at Linköping University (Faculty Grant SFO-Mat-LiU No. 2009-00971) and the Swedish e-Science Centre (SeRC), Knut & Alice Wallenberg Foundation New States of Matter 2014-2019 (COTXS), the Swedish Research Council (VR) Grants No. 621-2011-4426 and 2016-04810, the Swedish National Infrastructure for Computing Grants No. SNIC 001/12-275 and No. SNIC 2013/1-331, and the “Lendület program” of Hungarian Academy of Sciences is acknowledged. Support provided by the Ministry of Education and Science of the Russian Federation (Grant No. 14.Y26.31.0005) is gratefully acknowledged. Use of the Center for Nanoscale Materials was supported by the U. S. Department of Energy, Office of Science, Office of Basic Energy Sciences, under Contract No. DE-AC02-06CH11357.

* joel.davidsson@liu.se

¹ M. Lannoo, *Point defects in semiconductors I: theoretical aspects*, Vol. 22 (Springer Science & Business Media, 2012).

² J. Bourgoin, *Point defects in Semiconductors II: Experimental aspects*, Vol. 35 (Springer Science & Business Media, 2012).

³ L. Childress, J. M. Taylor, A. S. Sørensen, and M. D. Lukin, *Phys. Rev. Lett.* **96**, 070504 (2006).

⁴ I. Aharonovich, S. Castelletto, D. A. Simpson, A. Stacey, J. McCallum, A. D. Greentree, and P. S., *Nano Letters* **9**, 3191 (2009).

⁵ R. Kolesov, K. Xia, R. Reuter, R. Stöhr, A. Zappe, J. Meijer, P. R. Hemmer, and J. Wrachtrup, *Nature Communications* **3**, 1029 (2012).

- ⁶ S. Castelletto, B. C. Johnson, V. Ivády, N. Stavrias, T. Umeda, A. Gali, and T. Ohshima, *Nat. Mater.* **13**, 151 (2014).
- ⁷ *Nat Photon* **10**, 631 (2016).
- ⁸ F. Jelezko and J. Wrachtrup, *physica status solidi (a)* **203**, 3207 (2006).
- ⁹ R. Hanson and D. D. Awschalom, *Nature (London)* **453**, 1043 (2008).
- ¹⁰ D. D. Awschalom, L. C. Bassett, A. S. Dzurak, E. L. Hu, and J. R. Petta, *Science* **339**, 1174 (2013).
- ¹¹ L. du Preez, Ph.D. thesis, University of Witwatersrand (1965).
- ¹² G. Balasubramanian, P. Neumann, D. Twitchen, M. Markham, R. Kolesov, N. Mizuochi, J. Isoya, J. Achard, J. Beck, J. Tessler, V. Jacques, P. R. Hemmer, F. Jelezko, and J. Wrachtrup, *Nature Mater.* **8**, 383 (2009).
- ¹³ B. B. Buckley, G. D. Fuchs, L. C. Bassett, and D. D. Awschalom, *Science* **330**, 1212 (2010).
- ¹⁴ L. Robledo, L. Childress, H. Bernien, B. Hensen, P. F. A. Alkemade, and R. Hanson, *Nature* **477**, 574 (2011).
- ¹⁵ J. J. L. Morton, A. M. Tyryshkin, R. M. Brown, S. Shankar, B. W. Lovett, A. Ardavan, T. Schenkel, E. E. Haller, J. W. Ager, and S. A. Lyon, *Nature* **455**, 1085 (2008).
- ¹⁶ A. Morello, J. J. Pla, F. A. Zwanenburg, K. W. Chan, K. Y. Tan, H. Huebl, M. Mottonen, C. D. Nugroho, C. Yang, J. A. van Donkelaar, A. D. C. Alves, D. N. Jamieson, C. C. Escott, L. C. L. Hollenberg, R. G. Clark, and A. S. Dzurak, *Nature* **467**, 687 (2010).
- ¹⁷ J. J. Pla, K. Y. Tan, J. P. Dehollain, W. H. Lim, J. J. L. Morton, D. N. Jamieson, A. S. Dzurak, and A. Morello, *Nature* **489**, 541 (2012).
- ¹⁸ W. F. Koehl, B. B. Buckley, F. J. Heremans, G. Calusine, and D. D. Awschalom, *Nature* **479**, 84 (2011).
- ¹⁹ A. L. Falk, B. B. Buckley, G. Calusine, W. F. Koehl, V. V. Dobrovitski, A. Politi, C. A. Zorman, P. X.-L. Feng, and D. D. Awschalom, *Nature Commun.* **4**, 1819.
- ²⁰ D. J. Christle, A. L. Falk, P. Andrich, P. V. Klimov, J. U. Hassan, N. T. Son, E. Janzén, T. Ohshima, and D. D. Awschalom, *Nat Mater* **14**, 160 (2015).
- ²¹ A. Sipahigil, K. D. Jahnke, L. J. Rogers, T. Teraji, J. Isoya, A. S. Zibrov, F. Jelezko, and M. D. Lukin, *Phys. Rev. Lett.* **113**, 113602 (2014).
- ²² T. Iwasaki, F. Ishibashi, Y. Miyamoto, Y. Doi, S. Kobayashi, T. Miyazaki, K. Tahara, K. D. Jahnke, L. J. Rogers, B. Naydenov, F. Jelezko, S. Yamasaki, S. Nagamachi, T. Inubushi, N. Mizuochi, and M. Hatano, *Scientific Reports* **5**, 12882 (2015).

- ²³ V. A. Soltamov, A. A. Soltamova, P. G. Baranov, and I. I. Proskuryakov, *Phys. Rev. Lett.* **108**, 226402 (2012).
- ²⁴ H. Kraus, V. A. Soltamov, D. Riedel, S. Váth, F. Fuchs, A. Sperlich, P. G. Baranov, V. Dyakonov, and G. V. Astakhov, *Nature Physics* **10**, 157 (2014).
- ²⁵ K. Szász, V. Ivády, I. A. Abrikosov, E. Janzén, M. Bockstedte, and A. Gali, *Phys. Rev. B* **91**, 121201 (2015).
- ²⁶ R. Kolesov, K. Xia, R. Reuter, M. Jamali, R. Stöhr, T. Inal, P. Siyushev, and J. Wrachtrup, *Phys. Rev. Lett.* **111**, 120502 (2013).
- ²⁷ J. J. Longdell, M. J. Sellars, and N. B. Manson, *Phys. Rev. Lett.* **93**, 130503 (2004).
- ²⁸ C. Clausen, I. Usmani, F. Bussières, N. Sangouard, M. Afzelius, H. de Riedmatten, and N. Gisin, *Nature* **469**, 508 (2011).
- ²⁹ H. de Riedmatten, M. Afzelius, M. U. Staudt, C. Simon, and N. Gisin, *Nature* **456**, 773 (2008).
- ³⁰ H. Seo, M. Govoni, and G. Galli, *Scientific Reports* **6**, 20803 (2016).
- ³¹ E. Janzén and B. Magnusson, in *Silicon Carbide and Related Materials 2004*, Materials Science Forum, Vol. 483 (Trans Tech Publications, 2005) pp. 341–346.
- ³² L. Gordon, A. Janotti, and C. G. Van de Walle, *Phys. Rev. B* **92**, 045208 (2015).
- ³³ A. L. Falk, P. V. Klimov, B. B. Buckley, V. Ivády, I. A. Abrikosov, G. Calusine, W. F. Koehl, A. Gali, and D. D. Awschalom, *Phys. Rev. Lett.* **112**, 187601 (2014).
- ³⁴ A. F. Kohan, G. Ceder, D. Morgan, and C. G. Van de Walle, *Phys. Rev. B* **61**, 15019 (2000).
- ³⁵ A. Janotti and C. G. Van de Walle, *Phys. Rev. B* **76**, 165202 (2007).
- ³⁶ S. Lany and A. Zunger, *Phys. Rev. B* **78**, 235104 (2008).
- ³⁷ P. Deák, B. Aradi, T. Frauenheim, E. Janzén, and A. Gali, *Phys. Rev. B* **81**, 153203 (2010).
- ³⁸ C. Freysoldt, B. Grabowski, T. Hickel, J. Neugebauer, G. Kresse, A. Janotti, and C. G. Van de Walle, *Rev. Mod. Phys.* **86**, 253 (2014).
- ³⁹ G. Ceder and K. Persson, *Scientific American* (Dec 2013) (2013).
- ⁴⁰ S. Curtarolo, G. L. Hart, M. B. Nardelli, N. Mingo, S. Sanvito, and O. Levy, *Nature materials* **12**, 191 (2013).
- ⁴¹ A. Gali, A. Gällström, N. Son, and E. Janzén, *Mater. Sci. Forum* **645-648**, 395 (2010).
- ⁴² M. W. Doherty, N. B. Manson, P. Delaney, F. Jelezko, J. Wrachtrup, and L. C. Hollenberg, *Physics Reports* **528**, 1 (2013), the nitrogen-vacancy colour centre in diamond.

- ⁴³ J. R. Maze, A. Gali, E. Togan, Y. Chu, A. Trifonov, E. Kaxiras, and M. D. Lukin, e-print arXiv: **quant-ph/1010.1338** (2010).
- ⁴⁴ M. W. Doherty, N. B. Manson, P. Delaney, and L. C. L. Hollenberg, *New Journal of Physics* **13**, 025019 (2011).
- ⁴⁵ P. Baranov, I. Il'in, E. Mokhov, M. Muzafarova, S. Orlinskii, and J. Schmidt, *JETP Letters* **82**, 441 (2005).
- ⁴⁶ N. Son, P. Carlsson, J. ul Hassan, E. Janzén, T. Umeda, J. Isoya, A. Gali, M. Bockstedte, N. Morishita, T. Ohshima, and H. Itoh, *Phys. Rev. Lett.* **96**, 055501 (2006).
- ⁴⁷ P. Hohenberg and W. Kohn, *Phys. Rev.* **136**, B864 (1964).
- ⁴⁸ W. Kohn and L. J. Sham, *Phys. Rev.* **140**, A1133 (1965).
- ⁴⁹ A. Gali, E. Janzén, P. Deák, G. Kresse, and E. Kaxiras, *Phys. Rev. Lett.* **103**, 186404 (2009).
- ⁵⁰ J. P. Perdew, K. Burke, and M. Ernzerhof, *Phys. Rev. Lett.* **77**, 3865 (1996).
- ⁵¹ R. Armiento and A. E. Mattsson, *Phys. Rev. B* **72**, 085108 (2005).
- ⁵² J. Heyd, G. E. Scuseria, and M. Ernzerhof, *J. Chem. Phys.* **118**, 8207 (2003).
- ⁵³ J. Heyd, G. E. Scuseria, and M. Ernzerhof, *J. Chem. Phys.* **124**, 219906 (2006).
- ⁵⁴ J. Heyd, J. E. Peralta, G. E. Scuseria, and R. L. Martin, *The Journal of Chemical Physics* **123**, 174101 (2005), <http://dx.doi.org/10.1063/1.2085170>.
- ⁵⁵ K. Szász, T. Hornos, M. Marsman, and A. Gali, *Phys. Rev. B* **88**, 075202 (2013).
- ⁵⁶ G. Kresse and J. Hafner, *Phys. Rev. B* **49**, 14251 (1994).
- ⁵⁷ G. Kresse and J. Furthmüller, *Phys. Rev. B* **54**, 11169 (1996).
- ⁵⁸ P. E. Blöchl, *Phys. Rev. B* **50**, 17953 (1994).
- ⁵⁹ G. Kresse and D. Joubert, *Phys. Rev. B* **59**, 1758 (1999).
- ⁶⁰ H. J. Monkhorst and J. D. Pack, *Physical review B* **13**, 5188 (1976).
- ⁶¹ V. Ivády, T. Simon, J. R. Maze, I. A. Abrikosov, and A. Gali, *Phys. Rev. B* **90**, 235205 (2014).
- ⁶² M. W. Doherty, V. V. Struzhkin, D. A. Simpson, L. P. McGuinness, Y. Meng, A. Stacey, T. J. Karle, R. J. Hemley, N. B. Manson, L. C. L. Hollenberg, and S. Prawer, *Phys. Rev. Lett.* **112**, 047601 (2014).
- ⁶³ A. L. Falk, P. V. Klimov, V. Ivády, K. Szász, D. J. Christle, W. F. Koehl, A. Gali, and D. D. Awschalom, *Phys. Rev. Lett.* **114**, 247603 (2015).